

Electronic Supplementary Information

Acyldiazone-based supramolecular assembly undergoing a converse sol-to-gel transition on *trans*→*cis* photoisomerization

*Zhao Gao,^a Fei Yan,^a Lulu Shi,^a Yifei Han,^b Shuai Qiu,^a Juan Zhang,^a Feng Wang,^b Si Wu,^b and Wei Tian^{*a}*

^aShaanxi Key Laboratory of Macromolecular Science and Technology, MOE Key Laboratory of Material Physics and Chemistry under Extraordinary Conditions, School of Chemistry and Chemical Engineering, Northwestern Polytechnical University, Xi'an 710072, P. R. China. E-mail: happytw_3000@nwpu.edu.cn

^bDepartment of Polymer Science and Engineering, University of Science and Technology of China, Hefei, Anhui 230026, P. R. China.

Table of Contents

1.	Materials and methods	S2
2.	Photoisomerization of acyldiazone-linked monomer 1-E	S4
3.	Light-induced sol-to-gel transition	S7
4.	Insights into the sol-to-gel transition mechanism	S12
5.	In situ sol-to-gel transition generated valves	S17
6.	Synthetic routes to the targeted monomers	S18
7.	References	S24

1. Materials and methods

Reagents and reactants: Compound **5**,¹ and compound **6**² (see Scheme S1) were synthesized according to the previously reported literature. Other reagents and solvents used in the experiments were purchased from commercial sources without further purification.

Measurements: ¹H and ¹³C NMR spectra were obtained from Bruker Avance 400 instruments. Matrix-assisted laser desorption/ionization time-of-flight mass spectrometry mass (MALDI-TOF-MS) measurements were recorded on a Bruker Autoflex Speed spectrometer with DCTB as the matrix. UV-vis spectra were performed on a Shimadzu UV-2600 spectrometer, equipped with an S-1700 Peltier-type temperature controller. Fluorescence spectra were recorded on a Hitachi F-4600 FL spectrophotometer. Transmission electron microscope (TEM) images were recorded on a JEM-2100 electron microscope. Scanning electron microscopy (SEM) experiments were performed on an FEI Verios G4 instrument. Dynamic light scattering (DLS) experiments were conducted on a Brookhaven BI-9000AT instrument. X-ray diffraction (XRD) experiments were performed with Anton Paar SAXSess mc² or SAXSpoint 2.0 small-angle X-ray scattering instruments with a Cu-K α X-ray source ($\lambda = 1.540598 \text{ \AA}$). Fourier transform infrared spectra (FTIR) were recorded on a Nicolet iS50 infrared spectrometer. Circular dichroism (CD) measurements were performed on a Chirascan circular dichroism spectrometer. Rheological characterization was performed by using a TA ARG2 stress-controlled rheometer with 40 mm parallel plate geometry. The light-irradiated organogel was transferred onto the plate kept at 293 K. In order to avoid solvent evaporation, the surface of the sample between two plates was covered with glycerol. For light-induced gelation experiments, 365 nm UV lamp (irradiation intensities: 11.9 mW cm⁻²) was employed as the light source. For other photo-irradiation experiments, a hand-held UV lamp with 365 nm (irradiation intensities: 0.98 mW cm⁻²) light and 254 nm (irradiation intensities: 0.34 mW cm⁻²) light was employed as the light source. The irradiation intensities were measured by a CEL-NP2000-2 type actinometer.

Density functional theory (DFT) calculations: All of the optimized structures were performed on G09 software packages.³ During the DFT computations, all of the elements were described by the B3LYP/6-311G(d) computational method. The energy levels of HOMO and LUMO were obtained from optimized geometries. There are no imaginary frequencies for the optimized geometries. To reduce computational costs, the long alkyl chains in monomers are abbreviated as ethoxy groups.

Assembled structure calculations: The structures of octamers of **1-E** before and after photoirradiation were firstly drawn, respectively. The dispersion-corrected PM6-D3H4 semi-empirical method⁴

implemented in the MOPAC2016 program was used to optimize the geometry of the two octamers in vacuum. Frequency calculations were performed to demonstrate that all optimized geometries were absent of imaginary frequencies. The interaction regions and strength between the adjacent monomers were achieved by independent gradient model (IGM) isosurface analysis⁵ with Multiwfn program⁶. The IGM interaction regions and color mapped isosurface graphs of electrostatic potential were obtained by VMD program⁷. In the IGM analysis, the green isosurface color represents weak non-covalent interactions (such as van der Waals and π - π stacking interactions) while blue color denotes stronger interactions (such as hydrogen bonds).

Mathematical fitting of the supramolecular polymerization process of the light-irradiated **1:** The supramolecular polymerization process of light-irradiated **1** was described by a nucleation-elongation cooperative model, which was developed by Meijer, *et al.*⁸ This model was used to describe the supramolecular polymerization of light-irradiated **1** which exhibits a non-sigmoidal melting curve as shown in the temperature-dependent UV-vis spectra experiments. To acquire detailed thermodynamic parameters for the supramolecular polymerization process of light-irradiated **1**, the normalized UV-vis melting curves obtained by plotting the fraction of aggregated species (α_{agg} , $\lambda=418$ nm) against temperature were fitted with the mathematical model.

Microfluidic chips design and light-induced gel-based valve preparation: The three-layer microfluidic chips were prepared using 8.0 mm thick PMMA sheets as fluidic layers for liquid inlet/outlet and microchannels, 2.0 mm thick PMMA sheets as capping layer and a 300 μ m thick silicone film as sealing layer for sealing the chip. The Y-shape microchannel with two circular chambers (for filling the light-induced gel) and liquid inlet/outlet were micromilled on the fluidic layer and then sealed to the capping layer using the screws and nuts. The Y-shape microchannel dimensions were 1.0 mm wide and 300 μ m deep, while the circular chamber was 2.5 mm in diameter. The circular chamber in the Y-shape microchannel was filled initially with the pre-prepared high viscosity sol **1-E** by injection, and the gel-based valve was then created by irradiating the sol with 365 nm light. After creating the valve structure in situ within microfluidic chips, the one side microchannel is blocked and the fluid can only pass to the other side. The valve opening was achieved by gel-to-sol transition upon 254 nm light irradiation.

2. Photoisomerization of acylhydrazone-linked monomer 1-E

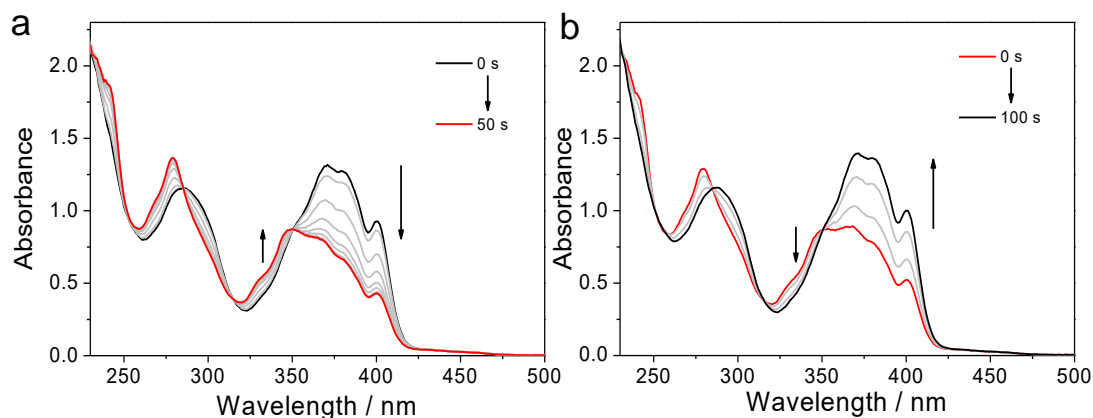


Figure S1. (a) UV-vis spectra change of **1-E** (5.0×10^{-5} M in DCE) upon 365 nm light irradiation. (b) UV-vis spectra change of **1-Z_{PSS}** (5.0×10^{-5} M in DCE) upon 254 nm light irradiation. Upon irradiation with 365 nm light for 50 s, the maximum absorption wavelength of **1-E** blue shifts from around 374 nm to 346 nm with concomitant two isosbestic points at 315 and 351 nm, revealing the *trans* to *cis* photoisomerization. Irradiation of the **1-Z_{PSS}** with 254 nm light regenerates the initial (*E*)-isomer, which is confirmed by the complete restoration of the absorption bands.

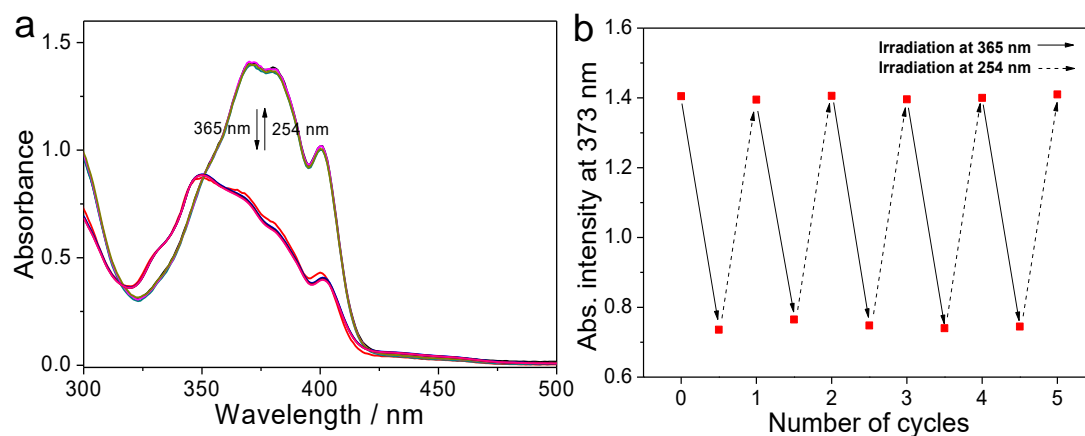


Figure S2. (a) UV-vis spectra change of **1-E** (5.0×10^{-5} M in DCE) upon the successive 365 nm and 254 nm light irradiation. (b) Multicycle experiments by monitoring the absorbance intensity changes at 373 nm. With the successive 365 nm and 254 nm light irradiation, the photoisomerization of **1** could be reversibly switched many times without noticeable degradation in performance.

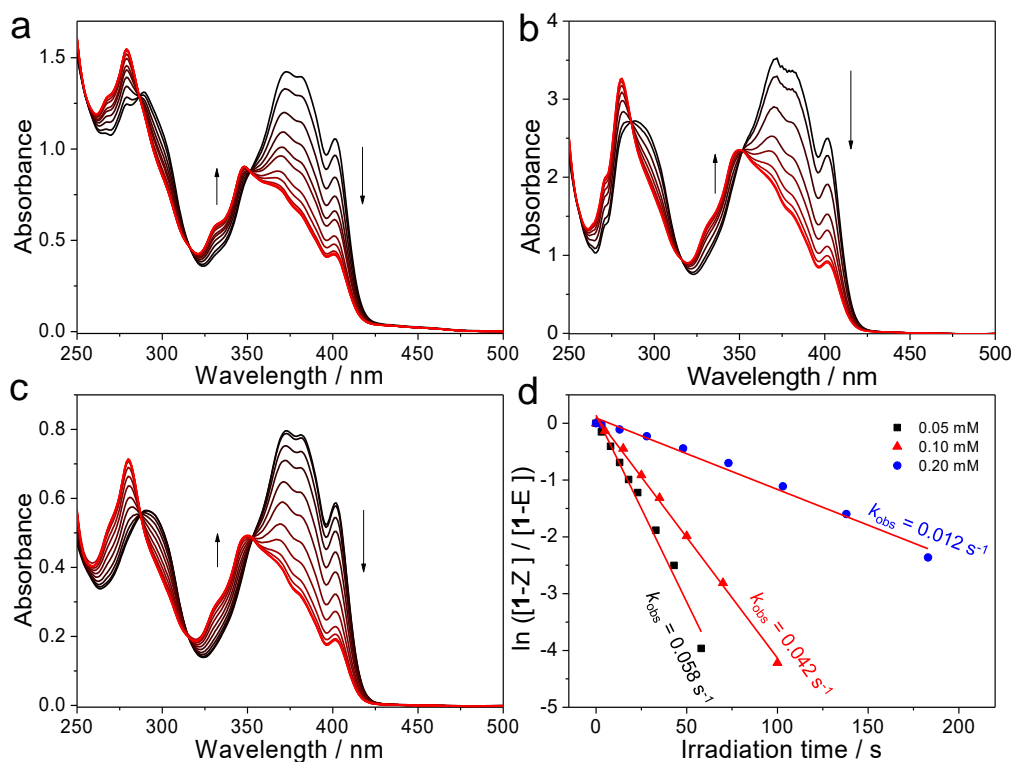


Figure S3. UV-vis spectra of **1-E** in DCE upon 365 nm light irradiation: (a) 5.0×10^{-5} M (optical path, $l = 10$ mm), (b) 1.0×10^{-4} M ($l = 10$ mm), and (c) 2.0×10^{-4} M ($l = 1$ mm). (d) Linear fitting of the photoisomerization of **1-E** ($\lambda_{\text{monitoring}} = 373$ nm). The photoisomerization rate (k_{obs}) is related to the concentration of **1-E**, which increases as the concentration increases.

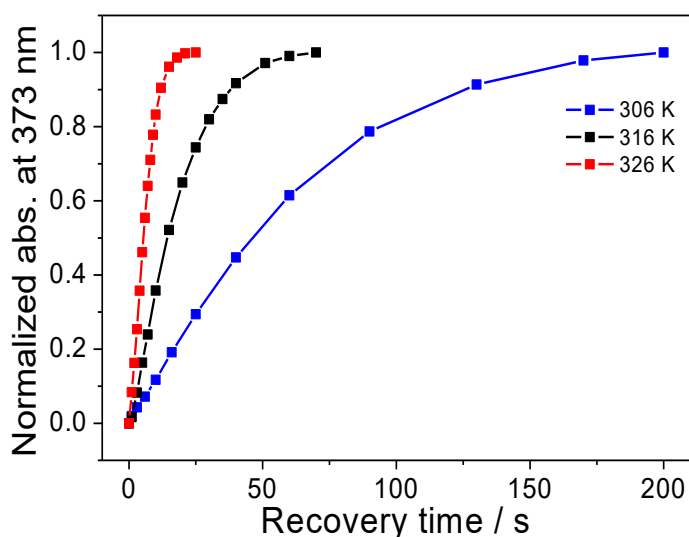


Figure S4. Normalized UV-vis spectra intensity of **1-Z_{PSS}** (5.0×10^{-5} M in DCE) at 373 nm *versus* time at different temperatures. In addition to 254 nm light irradiation, heating could also trigger the back-isomerization. Half-life time for the back-isomerization process was determined to be 5.4 s at 326 K, which can be modulated upon varying the temperature (14.7 s at 316 K and 46.1 s at 306 K).

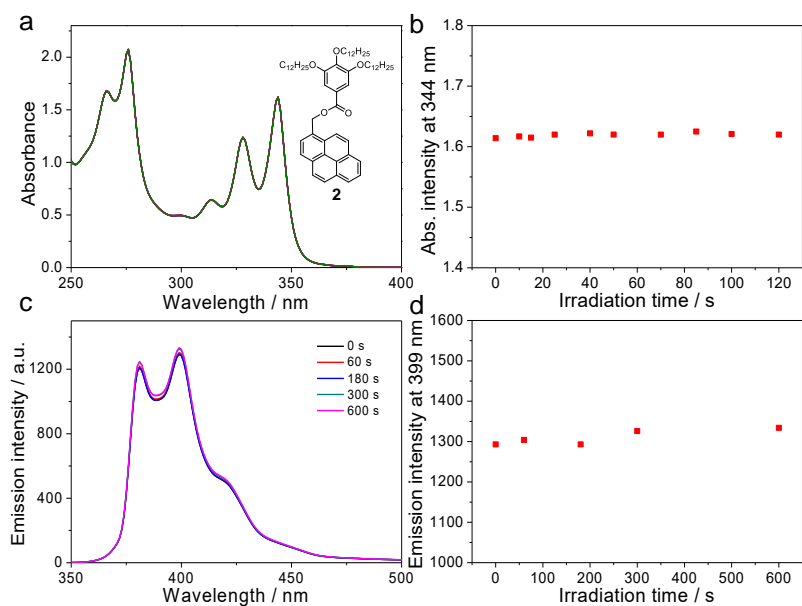


Figure S5. (a) UV-vis spectra change of **2** (5.0×10^{-5} M in DCE) upon 365 nm light irradiation, and (b) the corresponding intensity changes at 344 nm. (c) Fluorescence spectra change of **2** (5.0×10^{-5} M in DCE) upon 365 nm light irradiation, and (d) the corresponding intensity changes at 399 nm. $\lambda_{\text{ex}} = 340$ nm. The reference compound **2** (varying acylhydrazone unit of **1** to ester bond) is in disregard of the light irradiation, as evidenced by the almost complete lack of changes in the UV-vis and fluorescence signals.

3. Light-induced sol-to-gel transition

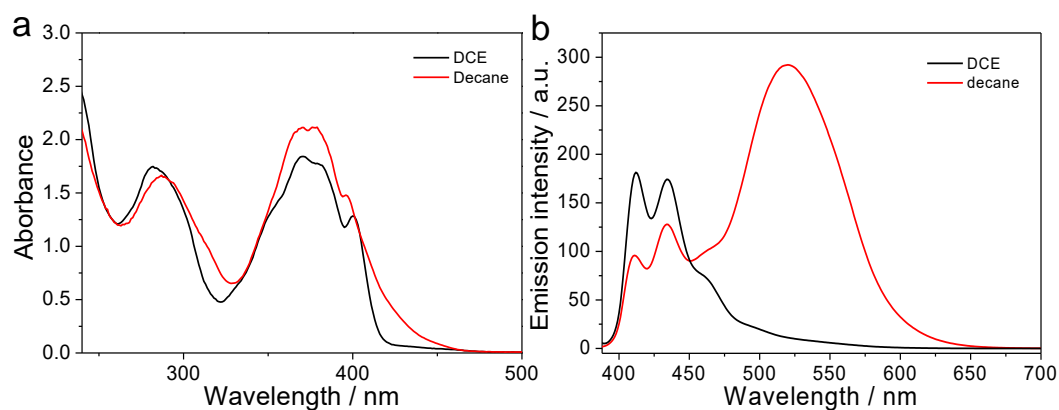


Figure S6. (a) UV-vis and (b) fluorescence spectra of **1-E** (5.0×10^{-5} M) in DCE and decane. $\lambda_{\text{ex}} = 369$ nm and 376 nm for **1-E** in DCE and decane, respectively.

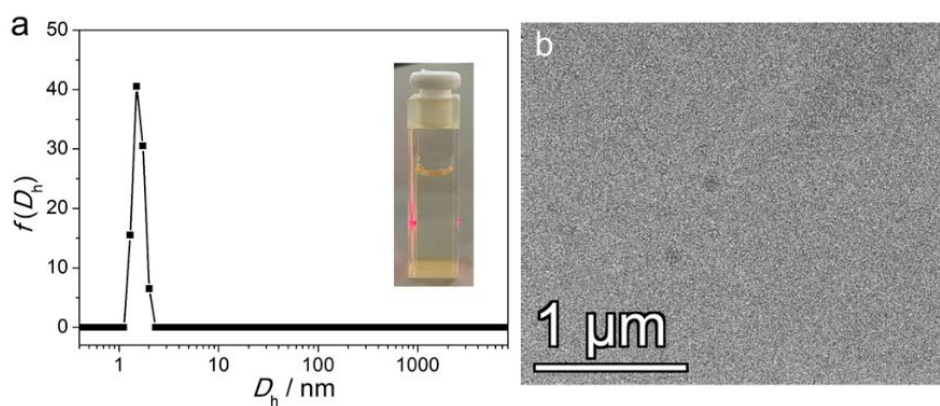


Figure S7. (a) DLS measurement of **1-E** (5.0×10^{-5} M) in decane. Inset: photograph of the decane solution of **1-E** irradiating with a laser pen. (b) TEM image of **1-E** on the copper grid.

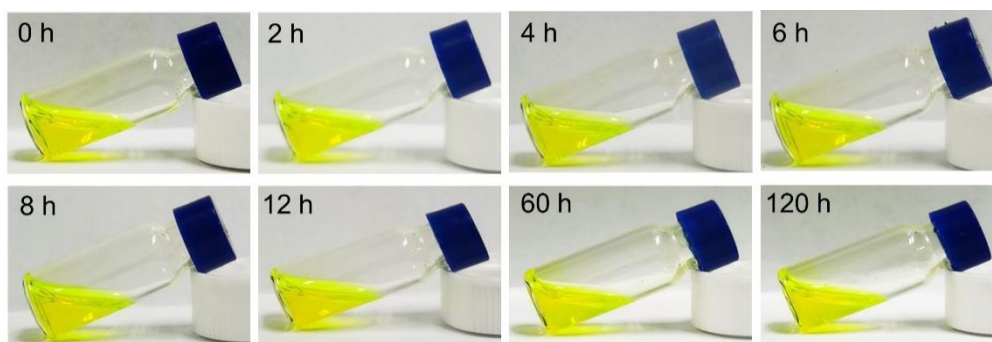


Figure S8. Images of the decane solution of **1-E** (20 mM, 298 K) upon keeping in a dark place for several days. Even increasing the concentration of **1-E** up to 20 mM, no gel can be visualized.

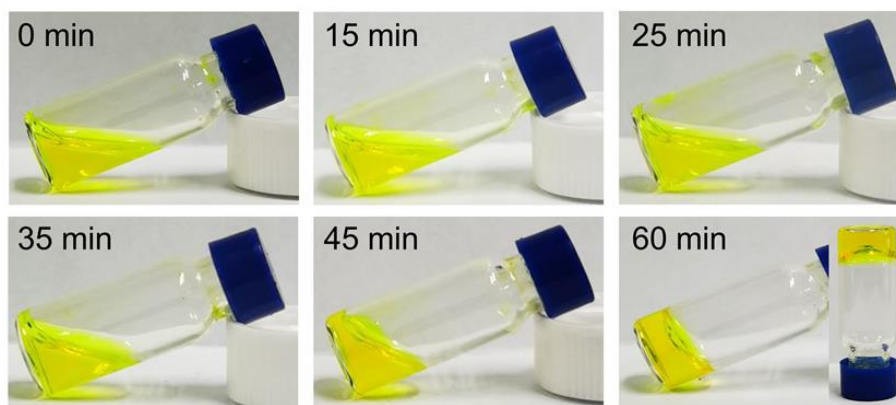


Figure S9. Images of the decane solution of **1-E** (10 mM, 298 K) upon 365 nm photoirradiation.

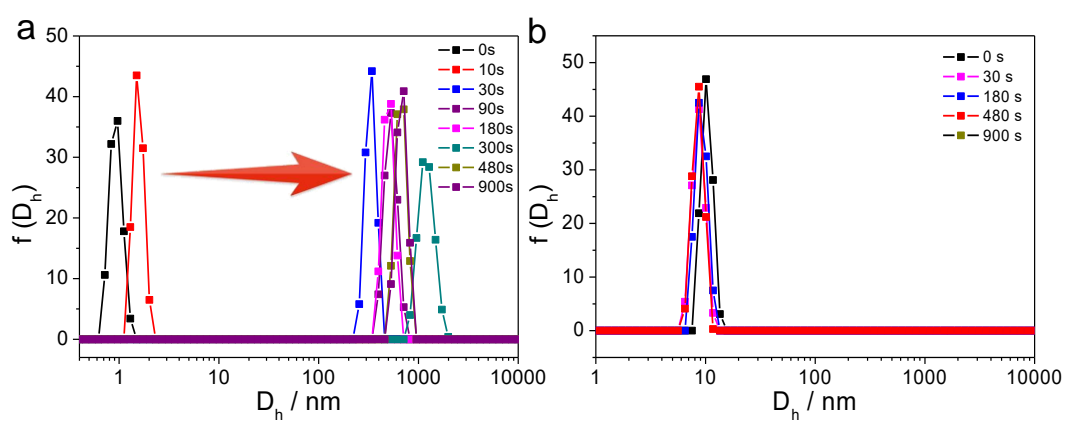


Figure S10. DLS curve variations of (a) **1-E** (5.0×10^{-5} M in decane) and (b) **2** (5.0×10^{-5} M in decane) upon 365 nm light irradiation.

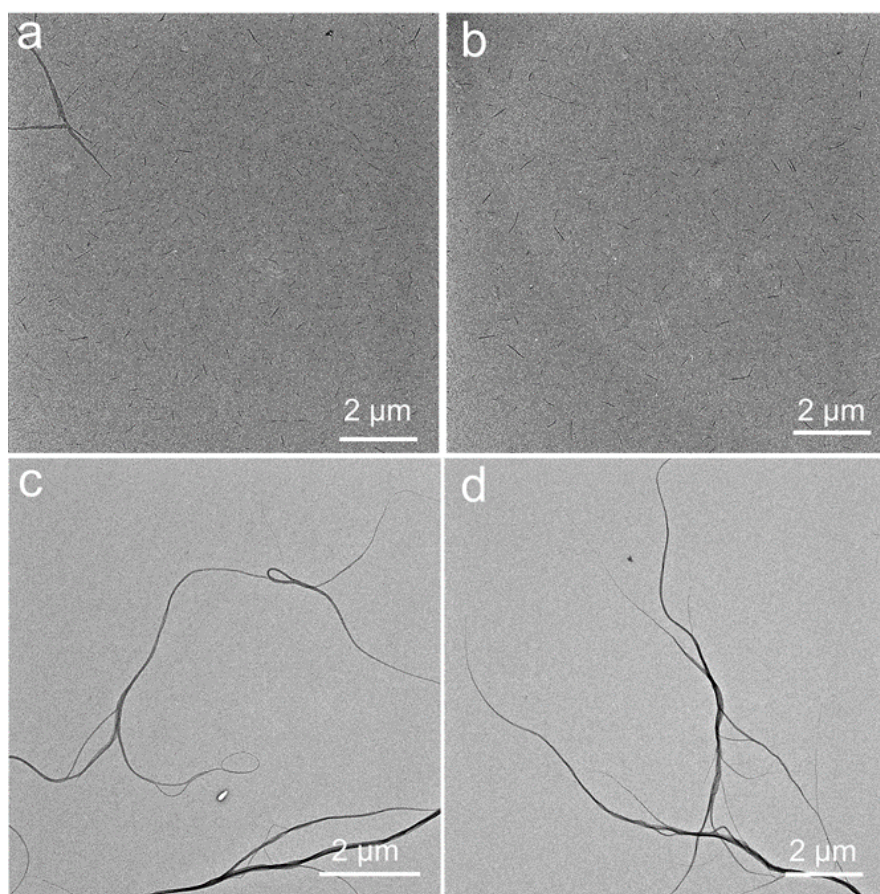


Figure S11. TEM micrographs of **1-E** (2.0×10^{-4} M in decane) after irradiation at 365 nm light for (a)–(b) 10 min, and (c)–(d) 30 min.

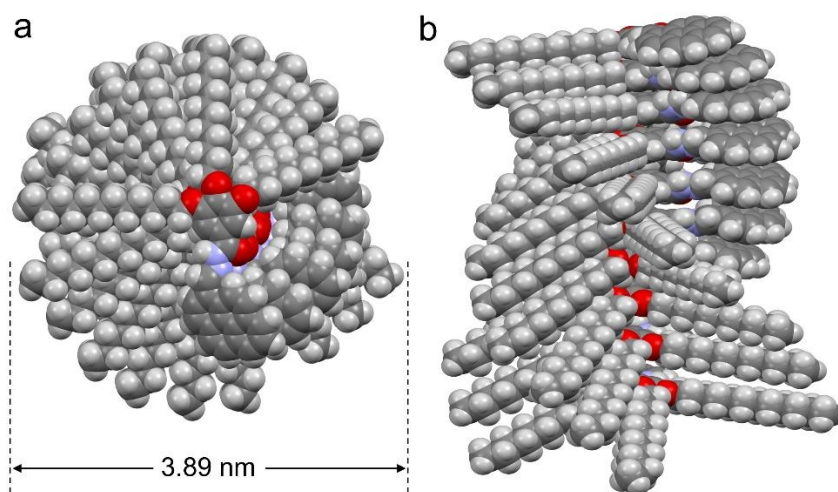


Figure S12. (a) Top view and (b) side view of the proposed stacking model of the light-irradiated **1-E**. The stacking model diameter of the light-irradiated **1-E** is calculated to be 3.89 nm, which is comparable to the lattice parameter ($a = 3.78$ nm) deduced from the diffraction maxima.

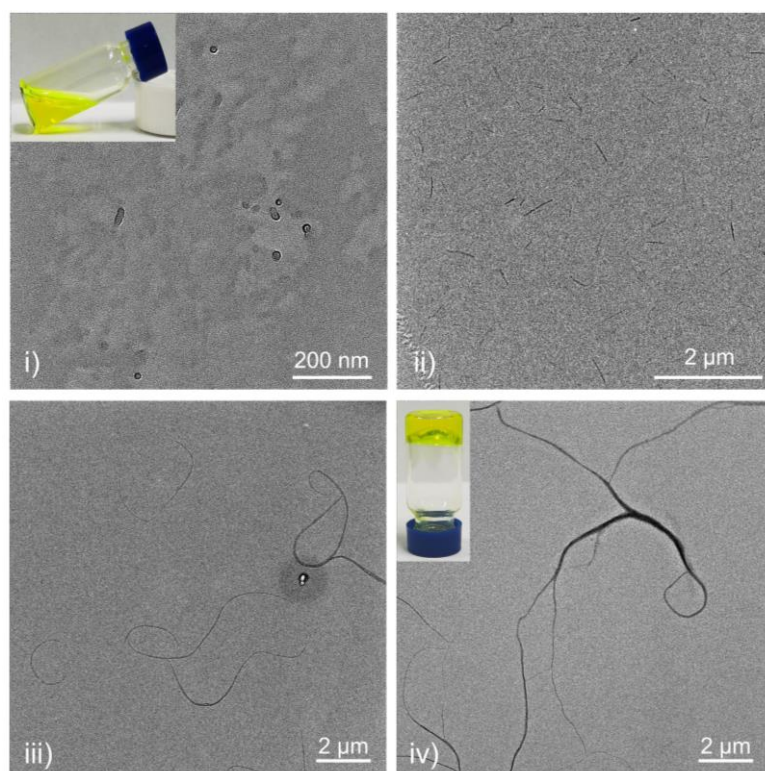


Figure S13. TEM micrographs of the diluted sol i) before, and after irradiation at 365 nm light for ii) 10 min, iii) 20 min, and iv) 30 min. Inset: i) sol was obtained when the gel was irradiated by 254 nm light; iv) gel was obtained again after the sol was irradiated with 365 nm light.

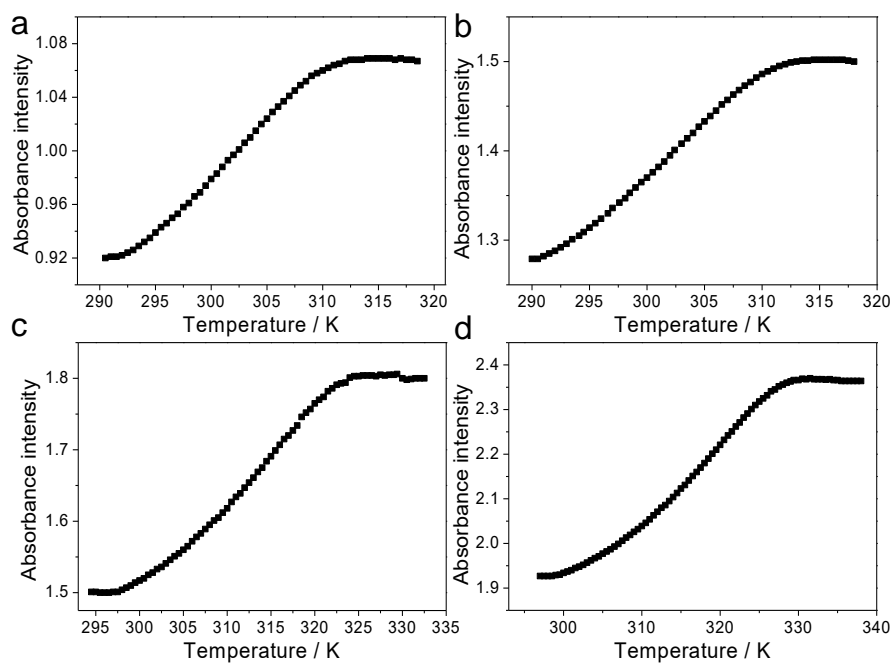


Figure S14. Temperature-dependent UV-vis absorption spectra of the light-irradiated **1-E** in decane: (a) 4.0×10^{-5} M; (b) 5.0×10^{-5} M; (c) 6.0×10^{-5} M; (d) 7.0×10^{-5} M. The absorbance intensities at $\lambda = 367$ nm display the non-sigmoidal cooling curves, which are characteristic for the cooperative nucleation–elongation mechanism.

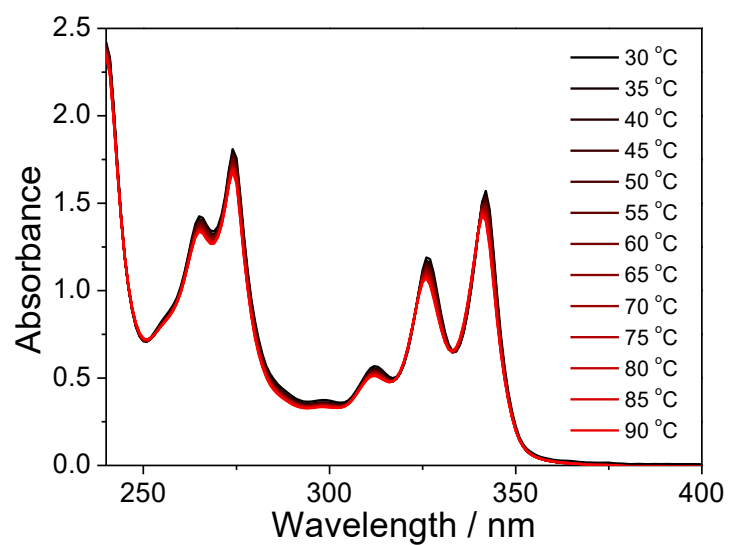


Figure S15. Temperature-dependent UV-vis absorption spectra of **2** (5.0×10^{-5} M) in decane. Only a small decrease of the absorbance intensity can be observed upon increasing the temperature, which indicates that compound **2** displays a rather weak self-assembly tendency.

4. Insights into the sol-to-gel transition mechanism

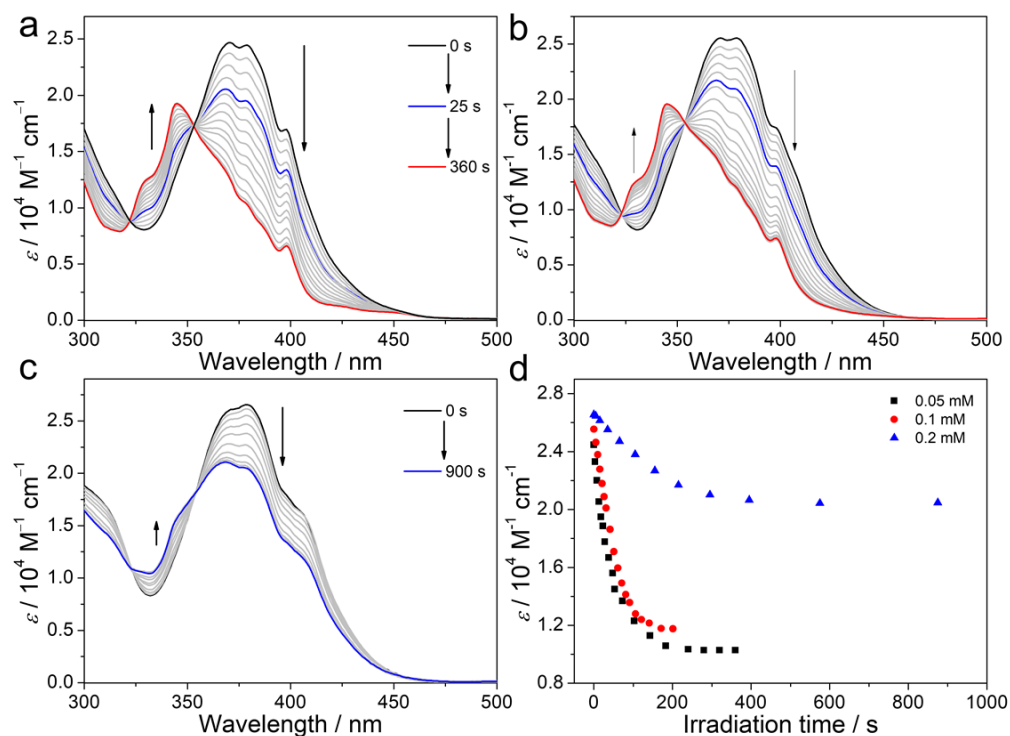


Figure S16. UV-vis spectra of **1-E** in decane upon 365 nm light irradiation: (a) 5.0×10^{-5} M, (b) 1.0×10^{-4} M, and (c) 2.0×10^{-4} M. (c) The relative *E-Z* conversion by monitoring the absorbance changes at 379 nm.

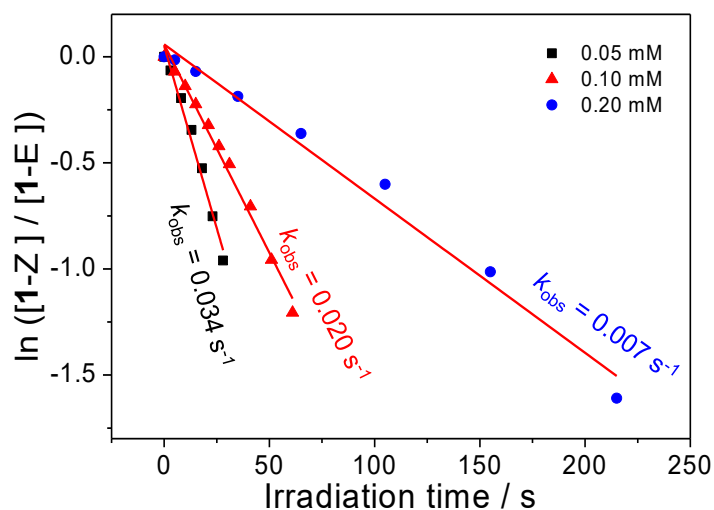


Figure S17. Linear fitting of the photoisomerization of **1-E** in decane at different concentrations upon 365 nm light irradiation ($\lambda_{\text{monitoring}} = 379$ nm). Due to the steric hindrance effect of stacked pyrene units, the k_{obs} in decane is slower than that in DCE.

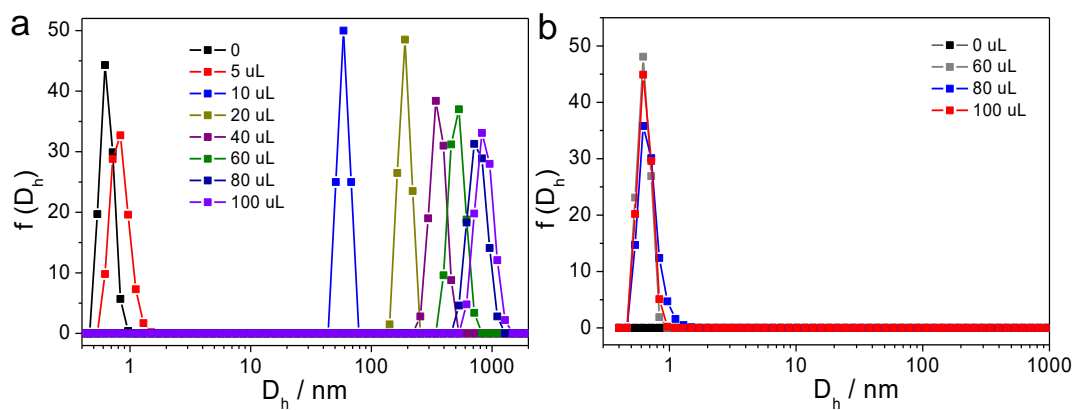


Figure S18. DLS hydrodynamic diameters variations upon gradual addition of **1-ZPSS** (2.0×10^{-4} M) into (a) the freshly prepared decane solution of **1-E** (2.0×10^{-4} M, 1 mL), and (b) pure decane solvent (1 mL).

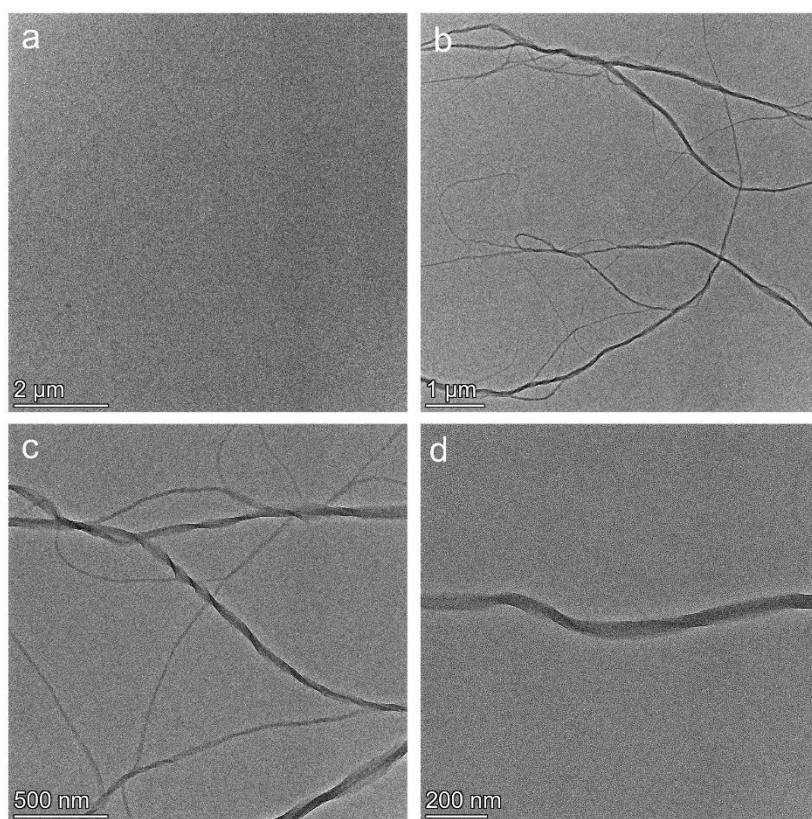


Figure S19. TEM micrographs of **1-E** (2.0×10^{-4} M in decane) (a) before, and (b)–(d) after adding 10 mol% of **1-ZPSS** (2.0×10^{-4} M in decane).

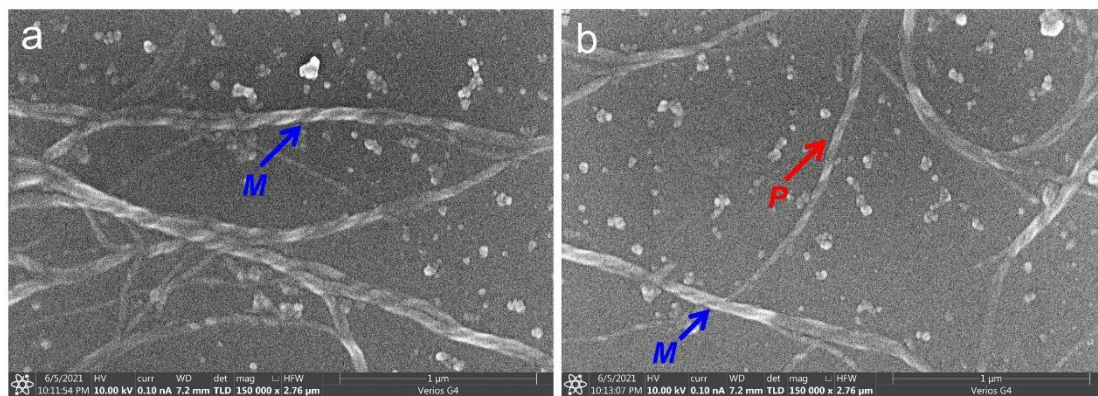


Figure S20. SEM micrographs of **1-E** (2.0×10^{-4} M in decane) after adding 10 mol% of **1-ZPSS** (2.0×10^{-4} M in decane). SEM images of the co-assemblies of **1-Z/1-E** showed that the fibers appeared as distinct right-handed (*P*) and left-handed (*M*) helical structures.

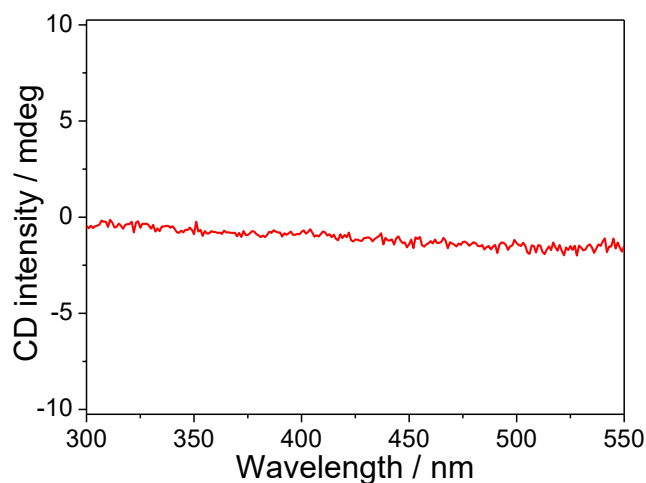


Figure S21. CD spectra of **1-E** (2.0×10^{-4} M in decane) after adding 10 mol% of **1-ZPSS** (2.0×10^{-4} M in decane). CD silence revealed the equal numbers of *P*- and *M*-type helical fibers

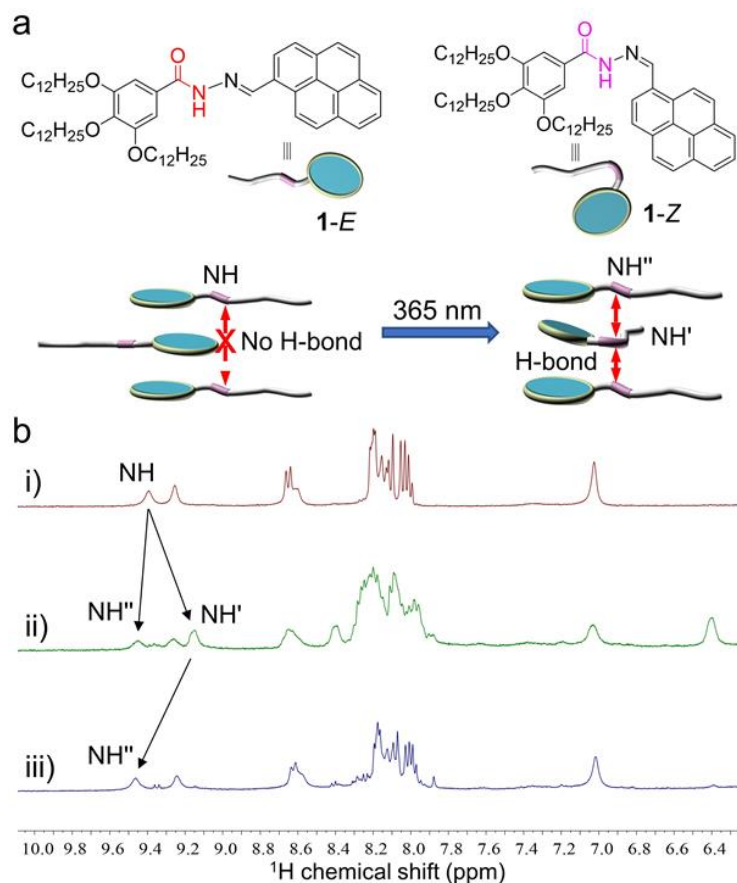


Figure S22. (a) Schematic illustration of monomers **1-E** and **1-Z**, and the proposed stacking mode for the assemblies before and after light irradiation. (b) Partial ¹H NMR spectra (C₂D₂Cl₄, 298 K, 2.00 mM) of **1-E**: i) before irradiation, ii) conversion to **1-Z_{PSS}** after 365 nm light irradiation, and iii) recovery to **1-E** upon 254 nm light irradiation. The arrow shows the changing of the NH proton.

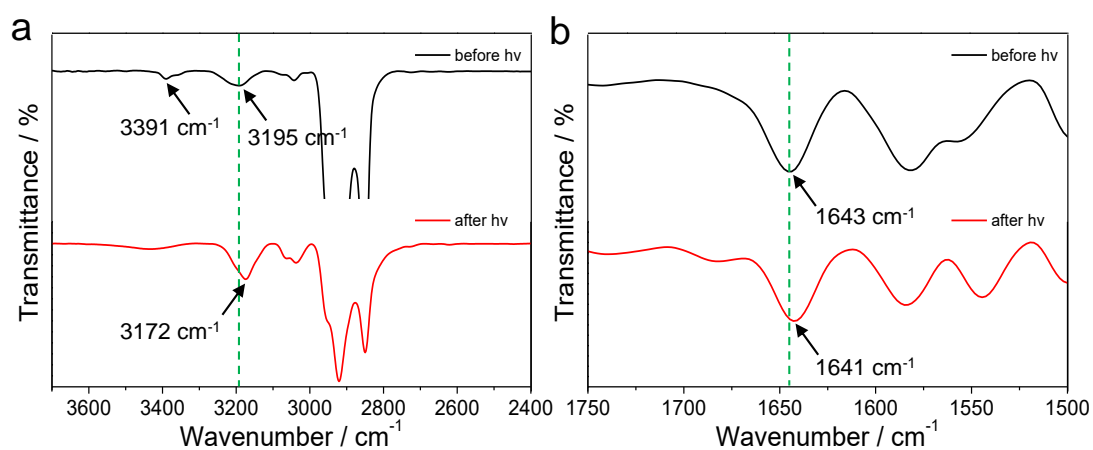


Figure S23. FTIR spectra collected from **1-E** before and after photoirradiation at 365 nm light.

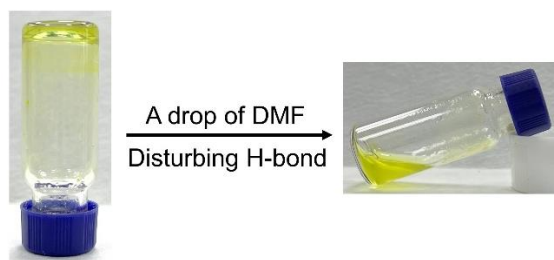
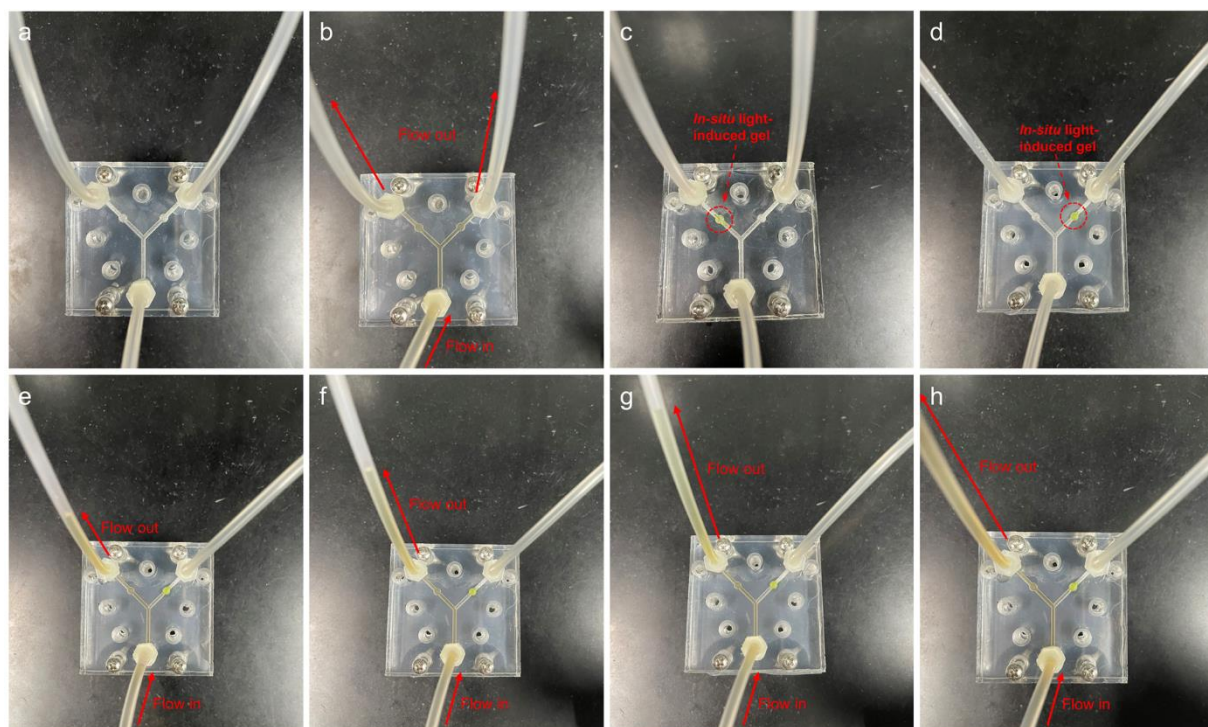
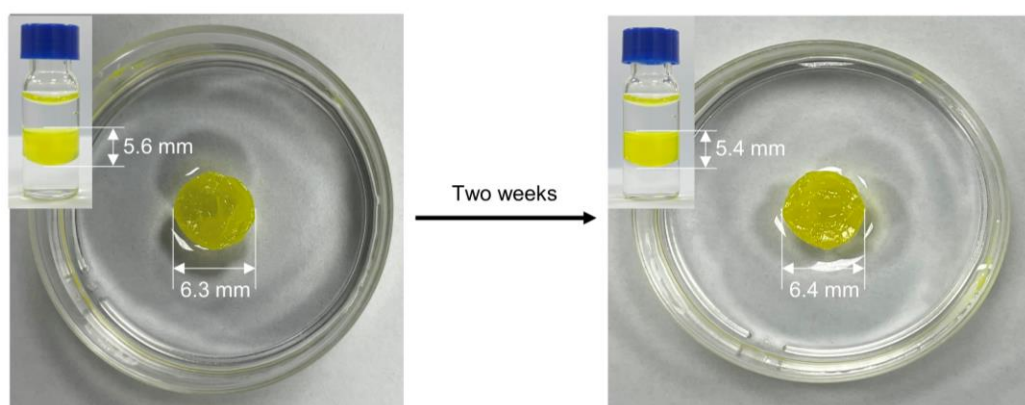


Figure S24. Images of **1-E** (20 mM) in decane before and after adding DMF solvent.

5. In situ sol-to-gel transition generated valves

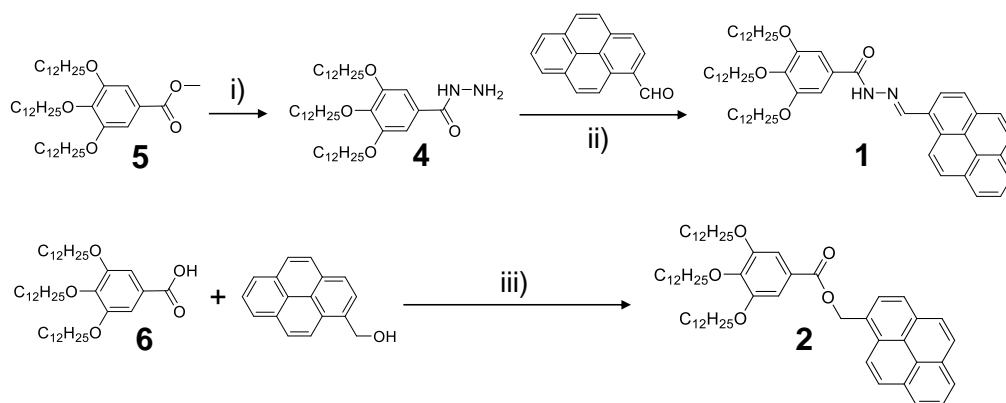


Supplementary Figure 25. Performance of the light-induced gel-based valves in water-based environment. Photographs of the microfluidic device: (a) before usage, (b) inletting water flow without valves, (c) and (d) in situ formed gel used as valve within the sealed PMMA chip, (e) no flow observed in the right side when the gel used as valve, and (f)–(h) the left side flow gradually increased.



Supplementary Figure 26. Photographs of the light-induced gel immersed and sandwiched in the saline solution before and after two weeks. The gel size remained unchanged (no swelling or shrinking).

6. Synthetic routes to the targeted monomers



Scheme S1. Synthetic routes to the targeted monomers. i) hydrazine hydrate, ethanol; ii) TFA, ethanol; iii) EDC, DMAP, CH₂Cl₂.

6.1 Synthesis of compound 4

3,4,5-trimethoxybenzohydrazide (500 mg, 2.21 mmol), hydrazine hydrate (5.53g, 110 mmol) were stirred in ethanol (20 mL). After refluxing at 100 °C for 12 hours, the reaction mixture was cooled to room temperature, suction filtration to obtain white filter residue, and wash the filter residue with ethanol three times to afford compound 4 as a white solid (452 mg, 90 %).⁹ ¹H NMR (400 MHz, CDCl₃) δ (ppm): 7.31 (s, 1H), 6.92 (s, 2H), 4.00–3.96 (m, 6H), 1.83–1.73 (m, 6H), 1.47–1.42 (m, 6H), 1.38–1.25 (m, 48H), 0.87 (t, *J* = 7.0 Hz, 9H).

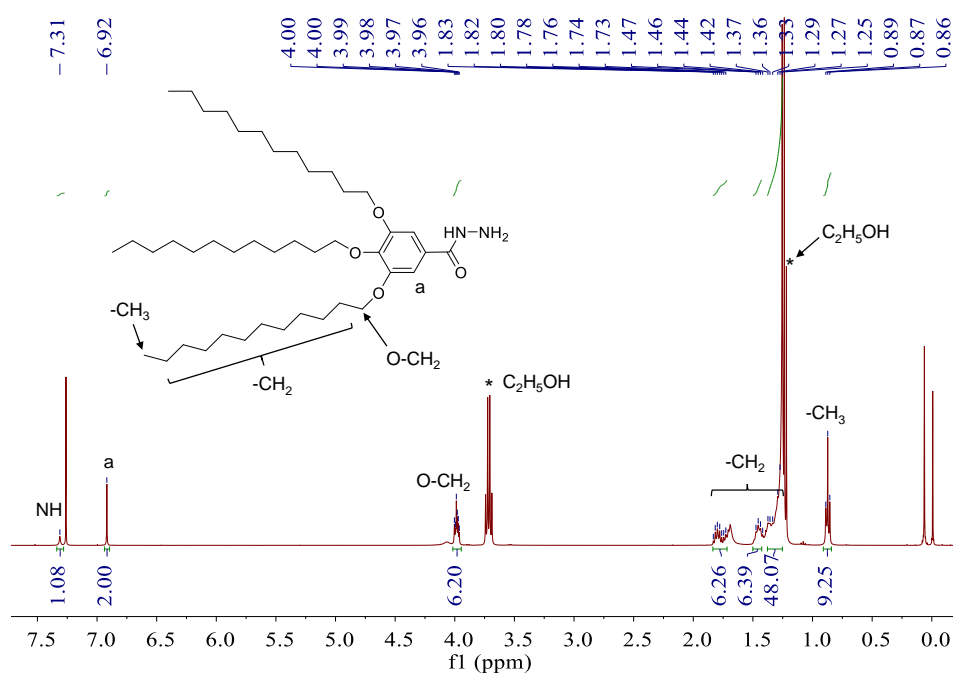


Figure S27. ¹H NMR spectrum (400 MHz, CDCl₃, 298 K) of compound 4.

6.2 Synthesis of monomer 1

Pyrene-1-carbaldehyde (59 mg, 0.26 mmol), compound **4** (58 mg, 0.26 mmol) and 3 drops of TFA were stirred in ethanol (20 mL). After stirring at 100 °C for 24 hours, the reaction mixture was cooled to room temperature, suction filtration to obtain white filter residue, wash the filter residue with ethanol for three times to afford monomer **1** as a yellow solid (100.74 mg, 88 %). ^1H NMR (400 MHz, CDCl_3) δ (ppm): 9.37 (s, 1H), 8.73 (d, $J = 9.3$ Hz, 1H), 8.35–7.98 (m, 9H), 7.14 (s, 2H), 4.06 (t, $J = 6.4$ Hz, 6H), 1.88–1.74 (m, 6H), 1.48 (s, 6H), 1.26 (d, $J = 6.3$ Hz, 48H), 0.90–0.85 (m, 9H). ^{13}C NMR (101 MHz, CDCl_3) δ (ppm): 164.69, 153.16, 147.32, 141.43, 132.39, 130.85, 130.11, 129.23, 128.17, 127.99, 127.03, 126.23, 125.68, 125.55, 125.22, 124.82, 124.27, 124.07, 121.67, 106.17, 73.50, 69.22, 31.92, 30.39, 29.77, 29.76, 29.73, 29.70, 29.67, 29.63, 29.48, 29.39, 29.38, 26.13, 26.10, 22.68, 14.10. MALDI-TOF-MS m/z : $[\text{M}+\text{H}]^+$, $\text{C}_{60}\text{H}_{89}\text{N}_2\text{O}_4$, calculated 901.6882; found 901.6680.

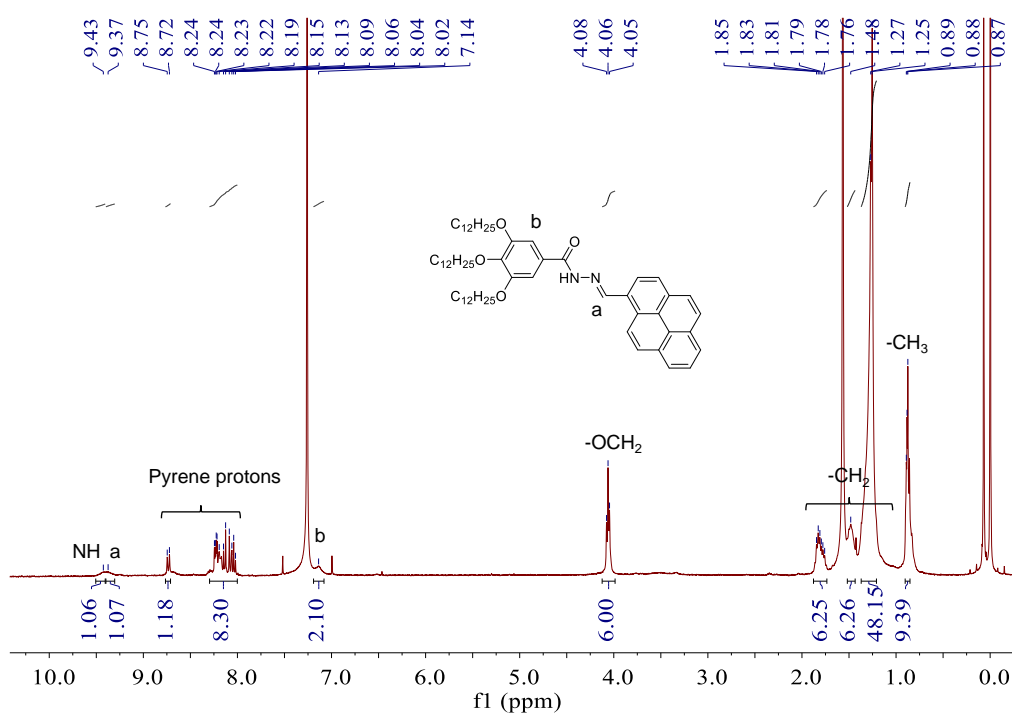
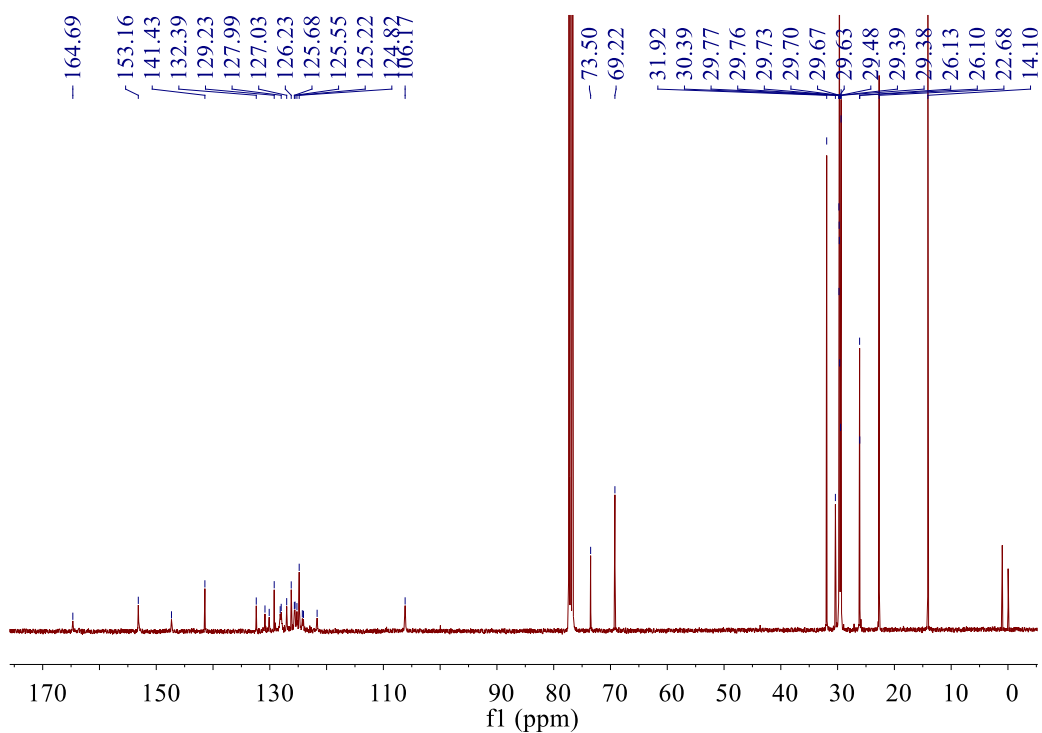
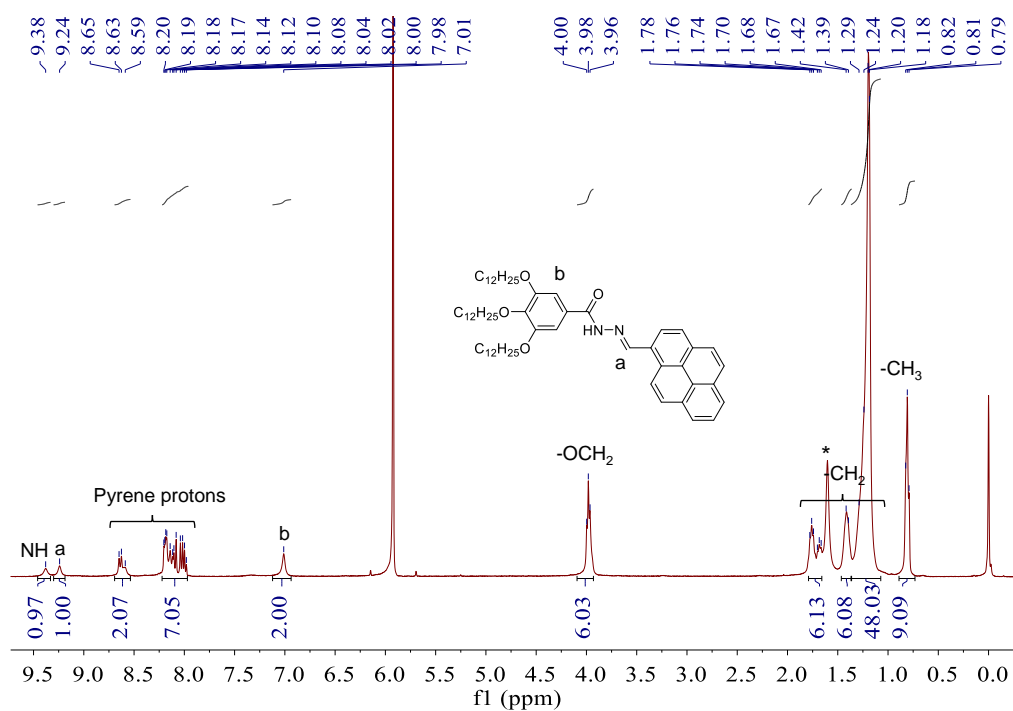


Figure S28. ^1H NMR spectrum (400 MHz, CDCl_3 , 298 K) of monomer **1**.



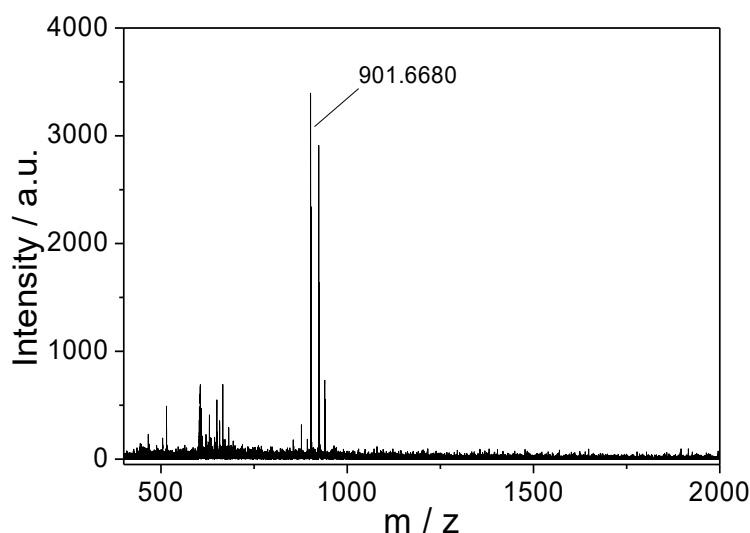


Figure S31. MALDI-TOF-MS spectrum of monomer **1**.

6.3 Synthesis of monomer **2**

3,4,5-tris(dodecyloxy)benzoic acid (100 mg, 0.15 mmol), pyren-1-ylmethanol (37.85 mg, 0.16 mmol), 1-(3-Dimethylaminopropyl)-3-ethylcarbodiimide hydrochloride (56.64 mg, 0.30 mmol) and 4-dimethylaminopyridine (25.3 mg, 0.21 mmol) were mixed in dichloromethane (20 mL). After stirring at room temperature for 12 hours, the mixture was extracted with H₂O/CH₂Cl₂ for three times. The combined organic extracts were dried over anhydrous Na₂SO₄, and the solvent was removed with a rotary evaporator. The residue was purified by flash column chromatography (petroleum ether/CH₂Cl₂, 30 : 1 v/v as the eluent) to afford monomer **2** as a white solid (116 mg, 87 %). ¹H NMR (400 MHz, CDCl₃) δ (ppm): 8.38 (d, *J* = 9.2 Hz, 1H), 8.23–8.00 (m, 8H), 7.31 (s, 2H), 6.06 (s, 2H), 3.98 (dt, *J* = 21.1, 6.5 Hz, 6H), 1.81–1.68 (m, 6H), 1.50–1.40 (m, 6H), 1.29 (d, *J* = 16.5 Hz, 48H), 0.90 (td, *J* = 6.8, 1.9 Hz, 9H). ¹³C NMR (101 MHz, CDCl₃) δ (ppm): 166.44, 152.80, 142.53, 131.72, 131.19, 130.69, 129.67, 129.04, 128.13, 127.80, 127.72, 127.34, 126.07, 125.50, 125.41, 124.91, 124.64, 124.59, 123.02, 108.18, 73.47, 69.15, 65.36, 31.91, 30.28, 29.72, 29.69, 29.67, 29.63, 29.59, 29.53, 29.35, 29.22, 26.02, 22.67, 14.10. MALDI-TOF-MS *m/z*: [M+H]⁺, C₆₀H₈₉O₅, calculated 889.6710; found 889.6787.

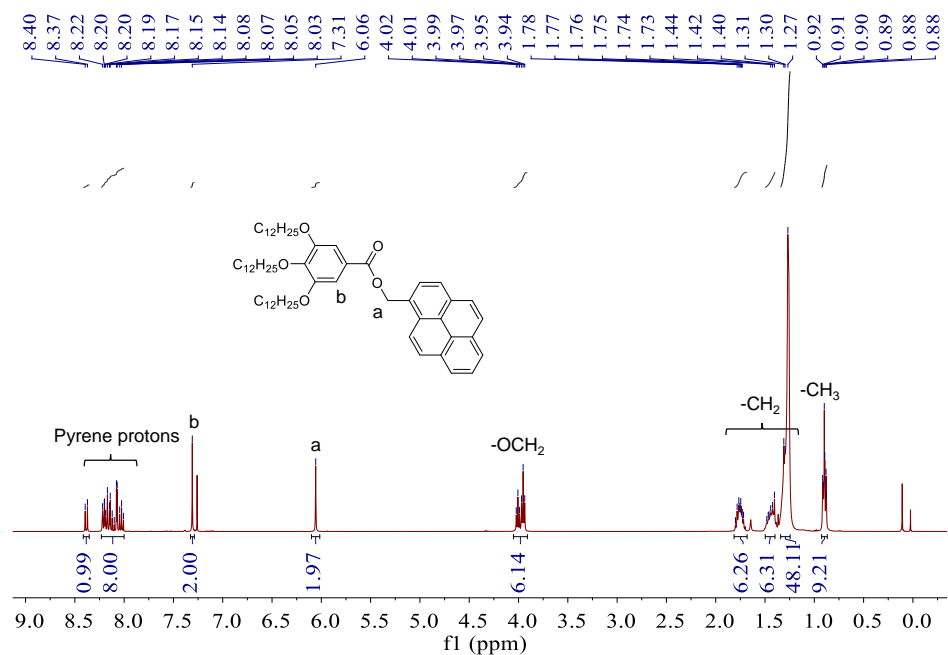


Figure S32. ¹H NMR spectrum (400 MHz, CDCl₃, 298 K) of monomer 2.

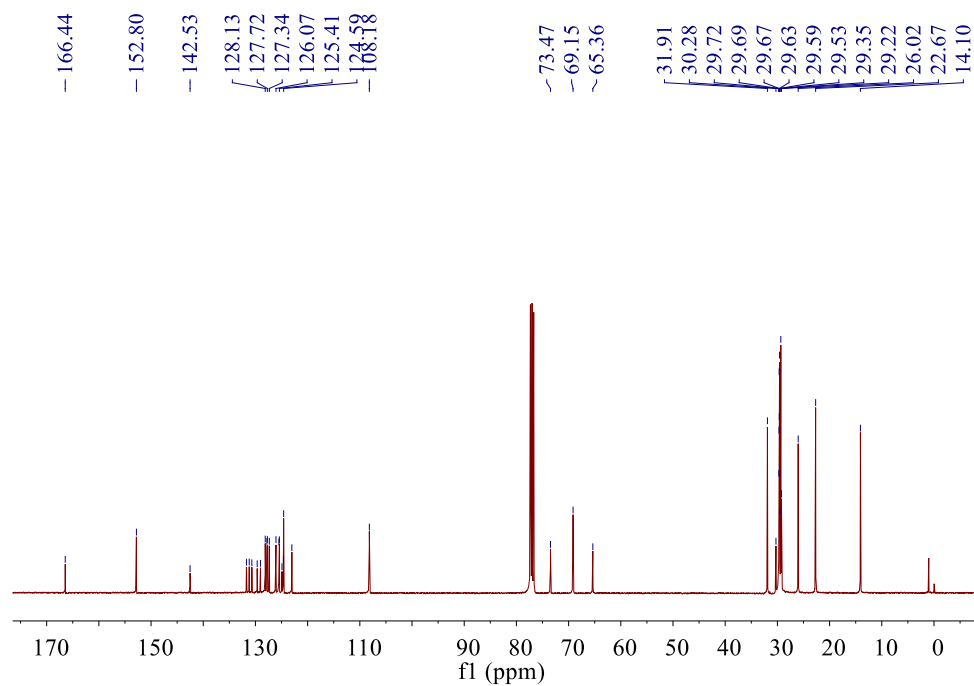


Figure S33. ¹³C NMR spectrum (101 MHz, CDCl₃, 298 K) of monomer 2.

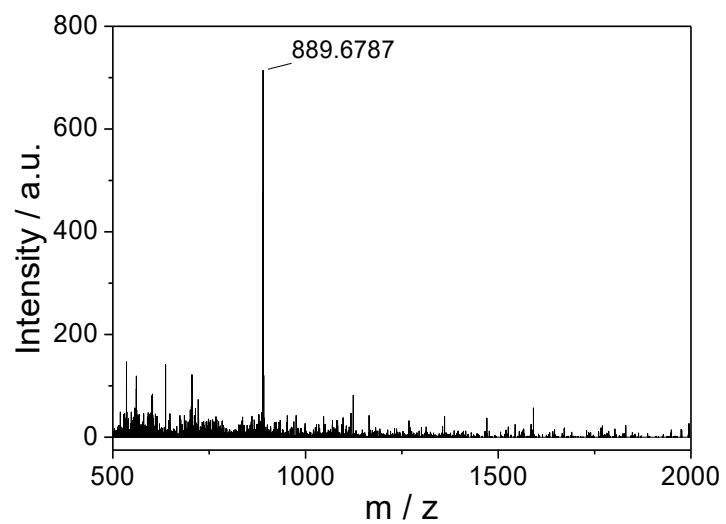


Figure S34. MALDI-TOF-MS spectrum of monomer **2**.

7. References

1. L.C. Lee and Y. Zhao, *J. Am. Chem. Soc.*, 2014, **136**, 5579–5582.
2. D. S. Janni and M. K. Manheri, *Langmuir*, 2013, **29**, 15182–15190.
3. Gaussian 09, Revision D.01, M. J. Frisch, et al. Gaussian, Inc., Wallingford CT, 2013.
4. J. Řezáč and P. Hobza, *J. Chem. Theory Comput.*, 2012, **8**, 141–151.
5. C. Lefebvre, G. Rubez, H. Khartabil, J. C. Boisson, J. Contreras-García and E. Hénon, *Phys. Chem. Chem. Phys.*, 2017, **19**, 17928–17936.
6. T. Lu and F. Chen, *J. Comput. Chem.*, 2012, **33**, 580–592.
7. W. Humphrey, A. Dalke and K. Schulten, *J. Mol. Graphics*, 1996, **14**, 33–38.
8. P. Jonkheijm, P. van der Schoot, A. P. H. J. Schenning and E. W. Meijer, *Science*, 2006, **313**, 80–83.
9. S. Mondal, P. Chakraborty, P. Bairi, D. P. Chatterjee and A. K. Nandi, *Chem. Commun.*, 2015, **51**, 10680–10683.